



## Article

# Magnetotransport Studies of Encapsulated Topological Insulator Bi<sub>2</sub>Se<sub>3</sub> Nanoribbons

Gunta Kunakova <sup>1,\*</sup> , Edijs Kauranens <sup>1</sup>, Kiryl Niherysh <sup>1,2</sup> , Mikhael Bechelany <sup>3</sup> , Krisjanis Smits <sup>4</sup> , Gatis Mozolevskis <sup>4</sup>, Thilo Bauch <sup>5</sup>, Floriana Lombardi <sup>5</sup> and Donats Erts <sup>1</sup>

<sup>1</sup> Institute of Chemical Physics, University of Latvia, 19 Raina Blvd., LV-1586 Riga, Latvia; edijs.kauranens@lu.lv (E.K.); kiryl.niherysh@lu.lv (K.N.); donats.erts@lu.lv (D.E.)

<sup>2</sup> Research and Development Department, Integrated Micro- and Nanosystems, Belarusian State University of Informatics and Radioelectronics, P. Brovki Str. 6, 220013 Minsk, Belarus

<sup>3</sup> Institut Européen des Membranes, IEM, UMR 5635, University of Montpellier, ENSCM, CNRS, 34095 Montpellier, France; mikhael.bechelany@umontpellier.fr

<sup>4</sup> Institute of Solid State Physics, University of Latvia, Kengaraga 8, LV-1063 Riga, Latvia; smits@cfi.lu.lv (K.S.); gatis.mozolevskis@cfi.lu.lv (G.M.)

<sup>5</sup> Quantum Device Physics Laboratory, Department of Microtechnology and Nanoscience, Chalmers University of Technology, SE-41296 Goteborg, Sweden; thilo.bauch@chalmers.se (T.B.); floriana.lombardi@chalmers.se (F.L.)

\* Correspondence: gunta.kunakova@lu.lv

**Abstract:** The majority of proposed exotic applications employing 3D topological insulators require high-quality materials with reduced dimensions. Catalyst-free, PVD-grown Bi<sub>2</sub>Se<sub>3</sub> nanoribbons are particularly promising for these applications due to the extraordinarily high mobility of their surface Dirac states, and low bulk carrier densities. However, these materials are prone to the formation of surface accumulation layers; therefore, the implementation of surface encapsulation layers and the choice of appropriate dielectrics for building gate-tunable devices are important. In this work, all-around ZnO-encapsulated nanoribbons are investigated. Gate-dependent magnetotransport measurements show improved charge transport characteristics as reduced nanoribbon/substrate interface carrier densities compared to the values obtained for the as-grown nanoribbons on SiO<sub>2</sub> substrates.

**Keywords:** Bi<sub>2</sub>Se<sub>3</sub> nanoribbons; ZnO; magnetotransport



**Citation:** Kunakova, G.; Kauranens, E.; Niherysh, K.; Bechelany, M.; Smits, K.; Mozolevskis, G.; Bauch, T.; Lombardi, F.; Erts, D.

Magnetotransport Studies of Encapsulated Topological Insulator Bi<sub>2</sub>Se<sub>3</sub> Nanoribbons. *Nanomaterials* **2022**, *12*, 768. <https://doi.org/10.3390/nano12050768>

Academic Editors: Yanquan Geng, Emmanuel Brousseau, Bo Xue, Jingran Zhang and Jiqiang Wang

Received: 27 January 2022

Accepted: 20 February 2022

Published: 24 February 2022

**Publisher's Note:** MDPI stays neutral with regard to jurisdictional claims in published maps and institutional affiliations.



**Copyright:** © 2022 by the authors. Licensee MDPI, Basel, Switzerland. This article is an open access article distributed under the terms and conditions of the Creative Commons Attribution (CC BY) license (<https://creativecommons.org/licenses/by/4.0/>).

## 1. Introduction

Three-dimensional topological insulators (3D-TIs) are among the major materials in the class of topological materials. 3D-TIs have attracted significant research interest due to their unusual surface properties. Carriers originating from topological surface states exhibit a Dirac cone in the band structure [1] and charge transport via these states is protected against backscattering from non-magnetic impurities [2,3]. If proximitized with an s-wave superconductor, superconductivity induced in the topological surface states is unconventional and predicted to host Majorana fermions [4,5]. The exploitation of these exotic surface properties is advantageous for a variety of applications, for example, in topological quantum computing [6], spintronics [7,8], and in the development of new-concept electronic devices [9]. The surface states of TIs are metallic while the bulk of the material, which is expected to be an insulator, is highly doped due to the formation of native defects [10]. This aspect remains the main challenge in accessing the surface-state charge transport, hampering progress towards the development of applications beyond fundamental studies.

Owing to their large surface-to-volume ratio, 3D-TI nanowires and nanoribbons are promising candidates with which to achieve truly topological surface-state-dominated charge transport without any contribution from the bulk. Their nanosized geometry provides even more functionalities because of the low number of transport modes [11], which

is particularly important for probing Majorana states [6]. Remarkable improvements in material quality have been demonstrated in 3D-TIs doped with native-defect-compensating substitutions. Nearly insulating bulk with a charge carrier density of  $\sim 10^{15} \text{ cm}^{-3}$  has been reported in single crystals of BiSbTeSe<sub>2</sub> [12] (BSTS), but this approach is not fully successful in nanowires and nanoribbons. Here, precise and reproducible concentrations of dopants are challenging to obtain, and they are achieved at the expense of charge carrier mobility [13].

Nanoribbons of Bi<sub>2</sub>Se<sub>3</sub> have been reported to be nearly ideal 3D-TIs, practically without any bulk conduction, and with exceptionally high carrier mobilities [14,15]. However, Bi<sub>2</sub>Se<sub>3</sub> is prone to the formation of surface accumulation layers [16]; this is particularly evident in thin nanoribbons, where the thickness is comparable with the Debye screening length [14,17,18]. The majority of the proposed 3D-TI-nanoribbon-based electronic devices require good tunability of their chemical potential for accessing surface Dirac carriers in a controlled manner. This can be achieved by employing electrostatic gating techniques. However, additional trivial carriers with large densities form at the nanoribbon surfaces, or at the interface with the substrate, which cannot be effectively depleted by common electrostatic gating techniques. Therefore, more effort is needed to prevent the uncontrolled formation of surface accumulation layers in Bi<sub>2</sub>Se<sub>3</sub> nanoribbons.

The use of surface-capping layers for Bi<sub>2</sub>Se<sub>3</sub> and Bi<sub>2</sub>Te<sub>3</sub> has proven to be beneficial to protect against environmental doping [19] and to probe surface state transport. Widely used capping layer materials are Te or Se, and the oxide layers of ZnO or Al<sub>2</sub>O<sub>3</sub> [13,20,21], deposited on the top surface of the material. This allows more efficient electrostatic tuning of the Fermi level [21], while in the case of Bi<sub>2</sub>Se<sub>3</sub> nanoribbons, where the accumulation layer is formed at the nanoribbon/substrate interface [14,17], other approaches have to be considered.

In this work, we used atomic layer deposition (ALD) to fabricate all-around ZnO-capped or -encapsulated Bi<sub>2</sub>Se<sub>3</sub> nanoribbons. The choice of selecting ZnO as an encapsulation layer material was based on the fact that thin layers of high-quality ZnO are possible to grow at moderate temperatures. This is particularly important for preserving the stoichiometry of Bi<sub>2</sub>Se<sub>3</sub>, as elevated temperatures may cause the unwanted out-diffusion of Se, which increases the doping of the bulk. Comparative magnetotransport studies of individual encapsulated and as-grown Bi<sub>2</sub>Se<sub>3</sub> nanoribbons from the same batch synthesis show that the encapsulation layer of ZnO helps to minimize the impact of the accumulation layer at the nanoribbon/substrate interface and improves the tunability of the chemical potential using a back-gate. These findings are important for the implementation of 3D-TI-nanoribbon-based topological quantum devices.

## 2. Materials and Methods

Free-standing Bi<sub>2</sub>Se<sub>3</sub> nanoribbons were grown on glass substrates using catalyst-free physical vapor deposition (PVD). The growth procedure is described in detail elsewhere [22]. As-grown nanoribbons were mechanically transferred to prepatterned Si/300 nm SiO<sub>2</sub> chips by bringing the chip and the glass substrate into contact with each other. The glass substrate with the remaining free-standing nanoribbons was then covered with 2 nm of ZnO, using ALD at  $\sim 100 \text{ }^\circ\text{C}$ , in a home-built set-up.

Flakes of hexagonal boron nitride (h-BN) were exfoliated from h-BN single crystals (2D semiconductors) and transferred to prepatterned Si/300 nm SiO<sub>2</sub> chips. ZnO-encapsulated Bi<sub>2</sub>Se<sub>3</sub> nanoribbons were then transferred to the chips partially covered with thin flakes of h-BN. Standard electron beam lithography processing was used to define electrical contacts to individual Bi<sub>2</sub>Se<sub>3</sub> and ZnO/Bi<sub>2</sub>Se<sub>3</sub> nanoribbons. After developing the resist, the samples were etched for 60 s in H<sub>2</sub>O/HCl/H<sub>2</sub>O<sub>2</sub>/CH<sub>3</sub>COOH solution [23] at room temperature to remove the surface oxide layer, and layers of Ti (3 nm) and Au (80 nm) were evaporated shortly after the etching to ensure formation of ohmic contacts.

Charge transport measurements were conducted in a Physical Property Measurement System (PPMS) Dynacool, equipped with a 9 T magnet, at a base temperature of 2 K. In

magnetoresistance measurements, a magnetic field  $B$  was applied perpendicularly to the nanoribbon surface. Electrode pair  $I^+/I^-$  (see Figure 2a) was used as the current electrodes to ensure a uniform flow of current in the nanoribbon, while the remaining electrodes  $V_1$  to  $V_8$  were employed as the voltage probes. Longitudinal resistance  $R_{xx}$  was recorded using, for example, electrode pair  $V_3/V_7$  while the transversal resistance  $R_{xy}$  was measured across the pair  $V_5/V_6$ . For this particular nanoribbon device, voltage electrodes  $V_1$  to  $V_4$  are positioned where the nanoribbon is on top of the h-BN flake ( $\sim 30$  nm in thickness), while the other voltage electrodes are located on the nanoribbon part, which is in direct contact with the  $\text{SiO}_2$ .

In order to determine whether the ZnO had covered the free standing  $\text{Bi}_2\text{Se}_3$  nanoribbons, the nanoribbons were transferred to Cu grids and imaged through high-resolution transmission electron microscope (HR-TEM Technai, Fei, Eindhoven, Netherland).

### 3. Results and Discussion

Simplified schematics illustrating the free-standing nanoribbons and encapsulation with a thin ZnO layer are shown in Figure 1a. The HR-TEM studies of the  $\text{ZnO}/\text{Bi}_2\text{Se}_3$  nanoribbons reveal a crystalline layer, with a thickness of  $\sim 2$  nm, at the nanoribbon surfaces. In total, five different nanoribbons of various geometries were examined, and a crystalline surface layer was formed in all of them. The  $d$ -spacing value estimated from the lattice fringes of  $\text{Bi}_2\text{Se}_3$  is 0.21 nm, which is in good agreement with the previous studies [22]. The  $d$ -spacing value determined for the ZnO of 0.28 nm corresponds to (100) planes of hexagonal wurtzite [24]. The interface between the  $\text{Bi}_2\text{Se}_3$  and ZnO is separated by a layer of amorphous material, with a thickness of  $\sim 1.5$ – $2$  nm. This layer corresponds to native oxide of  $\text{Bi}_2\text{Se}_3$ ,  $\text{BiO}_x$  (see Figure 1b), which is always present on surfaces of  $\text{Bi}_2\text{Se}_3$  [19].

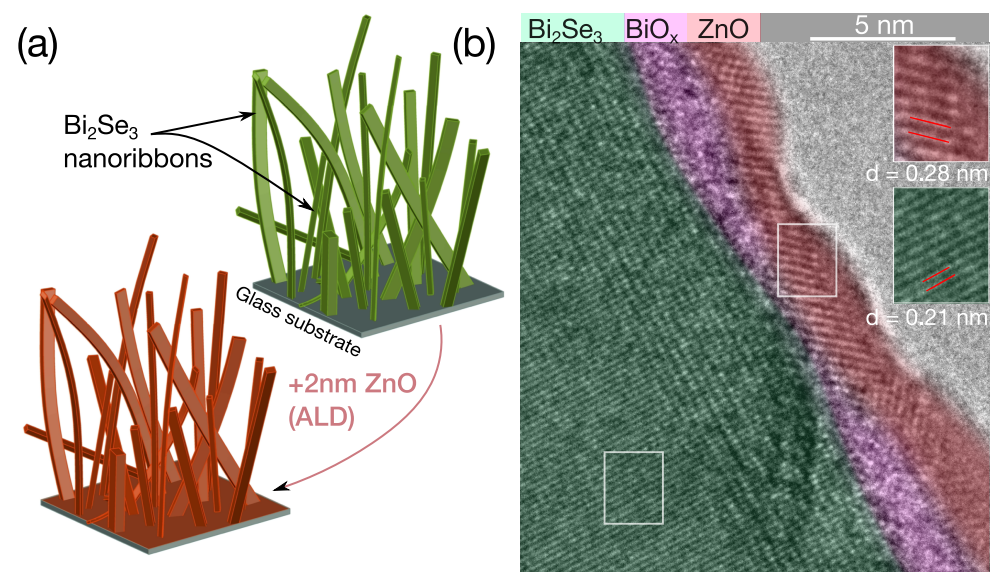


**Figure 1.** (a) Schematic representation of catalyst-free PVD-synthesized free-standing  $\text{Bi}_2\text{Se}_3$  nanoribbons on glass substrate; (b) false-colored HR-TEM image of a  $\text{Bi}_2\text{Se}_3$  nanoribbon after encapsulation with a thin layer of ZnO.

One of the fabricated nanoribbon Hall-bar devices used in the magnetotransport measurements is depicted in Figure 2a. The measured  $R_{xy}(B)$  at zero back-gate voltage is shown in Figure 2b. In order to minimize the error from misaligned electrodes, the data were anti-symmetrized as a function of the magnetic field (see inset of Figure 2b). The  $R_{xy}(B)$  dependences for all the measured nanoribbons were nonlinear. The absolute value of the slope calculated from the high magnetic field range 7–9 T was always smaller than the value determined from the 0–2.5 T range. This nonlinearity points to the charge carriers originating from two or more carrier bands characterised by different densities/mobilities.

The initial carrier density  $n_{3D}$  can be calculated from the low or high magnetic field slope of  $R_{xy}(B)$  as:

$$\frac{1}{n_{3D}e} = t \frac{dR_{xy}}{dB} \times \frac{w}{w_h}. \quad (1)$$

Here,  $t$  is the nanoribbon thickness,  $w$  is the nanoribbon width,  $w_h$  is the distance between the Hall contacts, and  $e$  is the elementary charge. The calculated values for the 2D carrier densities ( $n_{2D} = n_{3D} \cdot t$ ) from both the 0–2.5 T and 7–9 T regions for the as-grown and ZnO-encapsulated nanoribbons from the same batch synthesis are listed in Table S1 (see Supplementary Information (SI)). The values estimated from the 7–9 T range are about 20–30% higher than those obtained from the 0–2.5 T range.

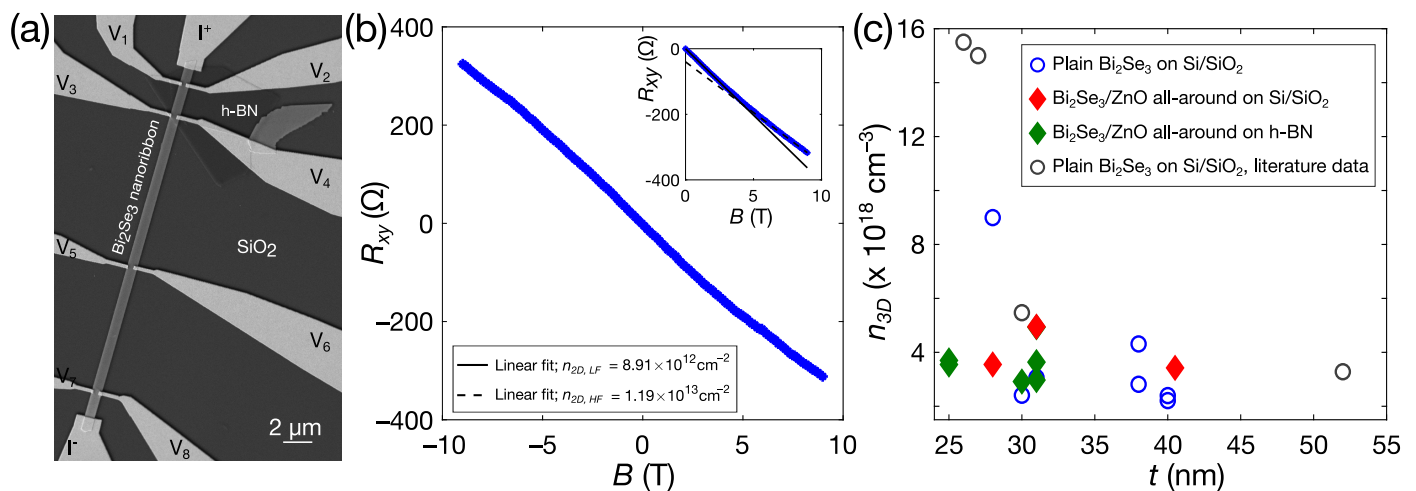


**Figure 2.** (a) SEM image of a  $\text{Bi}_2\text{Se}_3$  nanoribbon Hall-bar device; (b) Hall resistance  $R_{xy}(B)$  for the ZnO/ $\text{Bi}_2\text{Se}_3$  nanoribbon device A3t (see Table S1), measured at back-gate voltage  $V_g = 0$  V. The inset shows anti-symmetrized  $R_{xy}(B)$  data with linear fit in the 0–2.5 T range (black solid curve), and in the 7–9 T range (black dashed curve); (c) Hall carrier density of  $\text{Bi}_2\text{Se}_3$  and ZnO/ $\text{Bi}_2\text{Se}_3$  nanoribbons, plotted versus the nanoribbon thickness. In the case of the ZnO/ $\text{Bi}_2\text{Se}_3$  nanoribbons, total thickness  $t$  is reduced by 4 nm, accounting for the two  $\sim 2$  nm thick ZnO layers. Gray data points correspond to the data from [14]; here, the carrier density is calculated from the same magnetic field range (0–2.5 T).

Figure 2c shows the  $n_{3D}$  of the as-grown  $\text{Bi}_2\text{Se}_3$  and ZnO/ $\text{Bi}_2\text{Se}_3$  nanoribbons, plotted as a function of the nanoribbon thickness. The data correspond to the values calculated from the 0–2.5 T range, since in high magnetic fields, some nanoribbons showed the presence of Shubnikov–de Haas oscillations in  $R_{xx}(B)$ , additionally impacting the  $R_{xy}(B)$  dependence.

The charge carrier density  $n_{3D}$  for the as-grown  $\text{Bi}_2\text{Se}_3$  nanoribbons with thicknesses of  $\sim 30$ – $40$  nm is about  $\sim 3.5 \times 10^{18} \text{ cm}^{-3}$ , and it increases to  $\sim 9 \times 10^{18} \text{ cm}^{-3}$  for the 28-nanometer-thin nanoribbon. This peculiar  $n_{3D}(t)$  dependence of the catalyst-free PVD-grown  $\text{Bi}_2\text{Se}_3$  nanoribbons has been reported previously [14]. The increased 3D charge carrier density for nanoribbons of thicknesses below  $\sim 30$  nm is due to the accumulation layer of a large carrier density of  $\sim 1.3 \times 10^{13} \text{ cm}^{-2}$  (see Table 1), formed at the nanoribbon's bottom surface/substrate interface [14]. Figure 2c also includes the values of the carrier densities reported in [14] (gray points). In this work, the obtained  $n_{3D}(t)$  for the as-grown ribbons is similar to those previously reported in the literature.

The  $n_{3D}$  values for the ZnO-encapsulated  $\text{Bi}_2\text{Se}_3$  nanoribbons are close to those determined for the as-grown nanoribbons with thicknesses of  $\sim 30$ – $40$  nm, and are also about  $\sim 3.5 \times 10^{18} \text{ cm}^{-3}$ . A pronounced increase of  $n_{3D}$  of the thin ZnO-encapsulated nanoribbons ( $t < 30$  nm) is not observed, indicating that the overall carrier density in the accumulation layer could be smaller compared to the as-grown  $\text{Bi}_2\text{Se}_3$  nanoribbons.

The charge carrier density  $n_{2D}$  as a function of the back-gate voltage  $V_g$  for a 28-nanometer-thin ZnO-encapsulated  $\text{Bi}_2\text{Se}_3$  nanoribbon on h-BN is plotted in Figure 3a.

The applied back-gate voltage directly affects the nanoribbon bottom surface/substrate interface, and at higher  $V_g$  values, some parts of the nanoribbon bulk as well. The slope of the  $n_{2D}(V_g)$  gives an indication of the capacitance of this field-effect device, and  $C \approx 6.2 \times 10^{-5} \text{ F/m}^2$ . In order to effectively deplete the majority of the initial carriers of  $\sim 9 \times 10^{12} \text{ cm}^{-2}$ , one would need to apply approximately twice as high a voltage to the back-gate, which is not feasible for this device. Nevertheless, the  $n_{2D}(V_g)$  data are helpful for the study of the properties of the nanoribbon/substrate interface. The  $R_{xx}(V_g)$  data of the same ribbon reflect the  $n_{2D}(V_g)$  characteristics (see inset of Figure 3a). The absence of maxima or saturation in the  $R_{xx}(V_g)$  indicates that the Fermi energy  $E_F$  remained above the Dirac point in the entire measured  $V_g$  range. To tune the  $E_F$  to the Dirac point, which is important for accessing the charge carriers exclusively from the surface Dirac states, ultra-thin ( $t \sim 10 \text{ nm}$ )  $\text{Bi}_2\text{Se}_3$  nanoribbons would be needed. Another aspect for improving the gate tunability is the thickness and permittivity of the gate dielectric, i.e., a thinner dielectric layer than the 32 nm of h-BN on 300 nm of  $\text{SiO}_2$  could be used ( $\epsilon \sim 3\text{--}4$ ), or, alternatively, one could choose a  $\text{SrTiO}_3$  substrate, in which the relative dielectric constant at low temperatures is in the order of  $10^3\text{--}10^4$ .

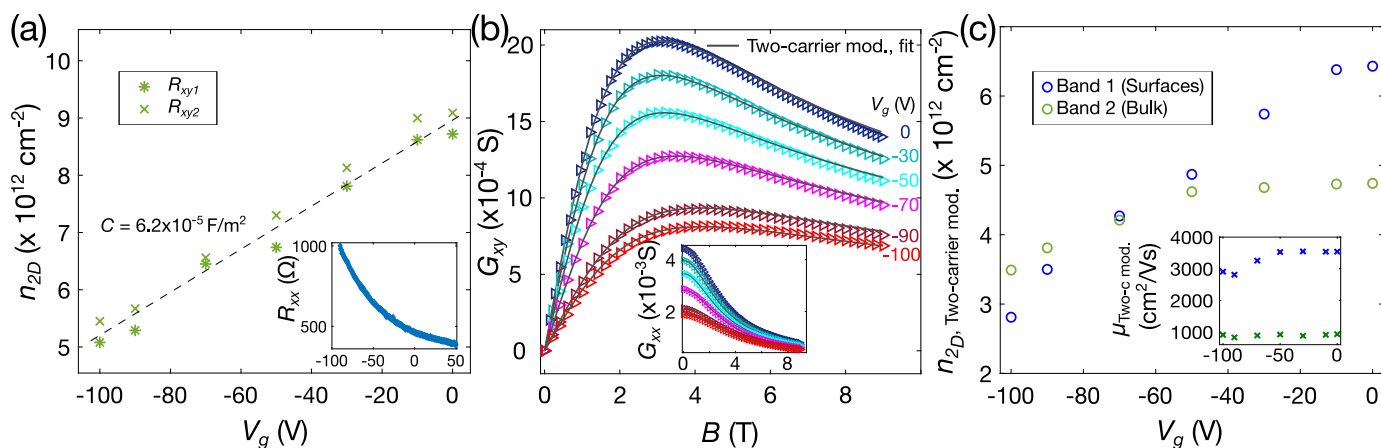


**Figure 3.** (a) Charge carrier density  $n_{2D}(=n_{3D}t)$  as a function of the back-gate voltage  $V_g$ . Here,  $n_{2D}$  is calculated from the anti-symmetrized  $R_{xy}(B)$  data in the 0–2.5 T range.  $R_{xy1}$  and  $R_{xy2}$  represent the Hall resistances measured using two different pairs of transversal electrodes, on the same nanoribbon. Black dashed line is the linear fit, and the capacitance estimated from the slope is  $6.2 \times 10^{-5} \text{ F/m}^2$ . In the inset—longitudinal resistance  $R_{xx}$  as a function of the  $V_g$ ; (b) conductance tensor element  $G_{xy}(B)$  at different applied  $V_g$ , fitted with the two-carrier model, inset shows fitted  $G_{xx}(B)$  curves; (c) from the two-carrier model extracted parameters of the two bands: carrier densities  $n_1; n_2$ , and mobilities  $\mu_1; \mu_2$  (in the inset) versus the back-gate voltage. All the data shown correspond to the  $\text{ZnO}/\text{Bi}_2\text{Se}_3$  nanoribbon A3t.

Since the  $R_{xy}(B)$  curves clearly indicate the presence of charge carriers from several carrier bands, we analysed the magnetotransport data using the two-carrier model.

Here, the conductance tensor elements  $G_{xy}$  and  $G_{xx}$  as a function of the magnetic field can be written as [25,26]:

$$G_{xy}(B) = eB \left( \frac{n_1\mu_1^2}{1 + \mu_1^2 B^2} + \frac{n_2\mu_2^2}{1 + \mu_2^2 B^2} \right) \tag{2a}$$

$$G_{xx}(B) = e \left( \frac{n_1\mu_1}{1 + \mu_1^2 B^2} + \frac{n_2\mu_2}{1 + \mu_2^2 B^2} \right) \tag{2b}$$

with parameters  $n_1, n_2$  and  $\mu_1, \mu_2$  representing the carrier densities and mobilities of the two bands, respectively.  $G_{xy}$  and  $G_{xx}$  from the measured resistances are calculated as:

$$G_{xy}(B) = -\frac{R'_{xy}}{R'^2_{xy} + R'^2_{xx}} \quad (3a)$$

$$G_{xx}(B) = -\frac{R'_{xx}}{R'^2_{xy} + R'^2_{xx}} \quad (3b)$$

$R'_{xy}$  is the Hall resistance, corrected considering the geometry of a nanoribbon Hall-bar device, and is equal to  $R_{xy} w/w_c$ .  $R'_{xx}$  is the sheet resistance, equal to  $R_{xx} w/L$ . The calculated conductance tensor elements as a function of magnetic field for different applied back-gate voltages are fitted with Equations (2a) and (2b) and plotted in Figure 3b. For the nanoribbon A3t, the extracted value of the charge carrier density of band 1 is  $n_1 = 6.43 \times 10^{12} \text{ cm}^{-2}$  and the mobility  $\mu_1 = 3530 \text{ cm}^2/\text{Vs}$ , while the carrier density and mobility of band 2 are  $n_2 = 4.74 \times 10^{12} \text{ cm}^{-2}$  and  $\mu_2 = 990 \text{ cm}^2/\text{Vs}$ , respectively. These parameters of the two bands are similar to those estimated for other ZnO-encapsulated  $\text{Bi}_2\text{Se}_3$  nanoribbons (see Table 1).

The extracted carrier density values  $n_1$  and  $n_2$  of the two bands change with the applied back-gate voltage. The value  $n_1$  scales linearly with the applied back-gate voltage and is reduced by  $\sim 50\%$  at  $V_g = -100 \text{ V}$ . Instead,  $n_2$  is practically insensitive to  $V_g$  in the  $0-50 \text{ V}$  range, while at  $V_g > -50 \text{ V}$  starts to decrease more rapidly.

**Table 1.** Summary of the carrier densities ( $\text{cm}^{-2}$ ) and mobilities ( $\text{cm}^2/\text{Vs}$ ) extracted from the two-band analysis and from the SdH oscillations for ZnO-encapsulated  $\text{Bi}_2\text{Se}_3$  nanoribbons on h-BN and  $\text{SiO}_2$  substrates, and comparison with the literature data (refs. [14,15,17]).

ZnO/ $\text{Bi}_2\text{Se}_3$ NR on h-BN:	$t_{NR}$ , nm	Surfaces (Band 1)		Bulk (Band 2)		Top Surface *	Bulk *
		$n_1$	$\mu_1$	$n_2$	$\mu_2$	$n_{2D, SdH}$	$n_{3D, SdH}$
A3t	29	$6.43 \times 10^{12}$	3540	$4.74 \times 10^{12}/1.64 \times 10^{18}$	930		
A1b	35	$7.18 \times 10^{12}$	4700	$5.31 \times 10^{12}/1.52 \times 10^{18}$	2052	$2.40 \times 10^{12}$	$1.44 \times 10^{18}$
D3b	34	$6.24 \times 10^{12}$	4800	$4.99 \times 10^{12}/1.46 \times 10^{18}$	1350		
$\text{Bi}_2\text{Se}_3$ NR on $\text{SiO}_2$ , sample E5 [14]	30	$15.0 \times 10^{12}$ **				$2.40 \times 10^{12}$	
$\text{Bi}_2\text{Se}_3$ NR on $\text{SiO}_2$ , sample BR3-10R2 [14]	63	-				$2.50 \times 10^{12}$	$1.70 \times 10^{18}$
$\text{Bi}_2\text{Se}_3$ NR on $\text{SiO}_2$ , sample E [17]	79	$13.0 \times 10^{12}$ *				$2.90 \times 10^{12}$	$6.60 \times 10^{17}$
$\text{Bi}_2\text{Se}_3$ NR on STO, sample B51-10 [15]	9	$5.55 \times 10^{12}$ **	1232				

\* Extracted from analysis of the SdH oscillations. \*\* These values account only carrier density of the nanoribbon bottom surface/substrate interface.

In what follows, we discuss a possible scenario that would account for this behaviour. Band 1 is affected by the back-gate voltage much more strongly; therefore, the carrier density  $n_1$  can most likely be associated with the surface states. As the nanoribbons are fully encapsulated by the ZnO protection layer, the mobilities of the nanoribbon top and bottom surfaces can be expected to have similar values, and carriers from both surfaces would appear in the same channel ( $n_1$ ) of the two-band model. The bulk mobilities are typically reported to be of much lower values [27], and the  $\mu_1$  of  $3530 \text{ cm}^2/\text{Vs}$  is more than three times larger than the value of  $\mu_2$ . For nanoribbon A1b, where the  $\mu_1$  is  $4700 \text{ cm}^2/\text{Vs}$ , SdH oscillations with two dominating frequencies are observed (see Figure S2, SI). One of the frequencies of  $\sim 99 \text{ T}$  is similar to that observed in the catalyst-free PVD-grown  $\text{Bi}_2\text{Se}_3$  nanoribbons, which have previously been reported to represent the surface Dirac states from the nanoribbon top surfaces [14,22,28]. This gives the carrier density of the nanoribbon top surface of  $n_{TS, SdH} \sim 2.4 \times 10^{12} \text{ cm}^{-2}$ . The carriers from the top surface are most likely insensitive to the back-gate voltage, as the nanoribbon is of a relatively large thickness. The

bottom surface/interface  $n_{BS, Int}$  carrier density at  $V_g = 0$  V would be then  $n_1 - n_{TS\ SdH} \approx 4 \times 10^{12} \text{ cm}^{-2}$ , which would not be very different from all the ZnO/Bi<sub>2</sub>Se<sub>3</sub> nanoribbons transferred onto the h-BN (4.03, 3.84 and  $4.78 \times 10^{12} \text{ cm}^{-2}$  for the nanoribbons A3t, D3b, and A1b, respectively). These low values corroborate that the ZnO encapsulation of Bi<sub>2</sub>Se<sub>3</sub> nanoribbons mitigates the creation of an accumulation layer.

Band 2 with carrier density  $n_2$  can be assumed to correspond to the bulk carriers. Above  $-50$  V, when the bottom surface/interface carriers are partly depleted, a fraction of the bulk carriers also starts to be affected by the back-gate voltage, and at  $V_g = -100$  V, the  $n_2$  is reduced to  $\sim 3.5 \times 10^{12} \text{ cm}^{-2}$ . At  $V_g = 0$  V, the  $n_2$  is  $4.74\text{--}5.31 \times 10^{12} \text{ cm}^{-2}$  (see Table 1), and if rescaling to the 3D values:  $1.46\text{--}1.64 \times 10^{18} \text{ cm}^{-3}$ . Peculiarly enough, the second frequency of the aforementioned SdH oscillations of the nanoribbon A1b (Figure S2, SI), with the highest  $\mu_2$ , gives  $1.44 \times 10^{18} \text{ cm}^{-3}$ . This value is close to the 3D bulk carrier densities determined from band 2.

#### 4. Conclusions

To conclude, the application of a ZnO encapsulation layer to topological insulator Bi<sub>2</sub>Se<sub>3</sub> nanoribbons and the use of h-BN as a substrate help to improve the nanoribbon/substrate interface properties. Thin layers of crystalline ZnO have no degrading impact on the overall transport characteristics of Bi<sub>2</sub>Se<sub>3</sub> nanoribbons. The 3D charge carrier densities for nanoribbons of different thicknesses are of the same order as the values determined for as-grown nanoribbons with thicknesses of 30–40 nm. The reduced surface carrier density extracted from two-band Hall analysis points towards a reduction in the interface accumulation layer when encapsulating Bi<sub>2</sub>Se<sub>3</sub> nanoribbons with a thin ZnO layer. Moreover, the ZnO-encapsulated nanoribbons show excellent Hall mobility. The presence of the Shubnikov–de Haas oscillations confirms that the high quality of catalyst-free PVD-grown Bi<sub>2</sub>Se<sub>3</sub> nanoribbons stays preserved if ZnO is used as an encapsulation layer. This approach of all-around encapsulation in combination with ultra-thin Bi<sub>2</sub>Se<sub>3</sub> nanoribbons, transferred to mono or few layer h-BN substrates, would be beneficial to controllably achieve ambipolar transport in Bi<sub>2</sub>Se<sub>3</sub>.

**Supplementary Materials:** The following supporting information can be downloaded at: <https://www.mdpi.com/article/10.3390/nano12050768/s1>.

**Author Contributions:** Conceptualization, G.K.; investigation E.K. and K.N.; resources K.S., G.M., T.B., F.L., D.E. and M.B.; writing—review and editing, G.K., T.B., F.L. and D.E. All authors have read and agreed to the published version of the manuscript.

**Funding:** This research was funded by the Latvian Council of Science, project “Highly tunable surface state transport in topological insulator nanoribbons”, No. lzp-2020/2-0343, and by the European Union’s Horizon 2020 research and innovation program, Grant Agreement No. 766714/HiTIME. Institute of Solid-State Physics, University of Latvia as the Center of Excellence has received funding from the European Union’s Horizon 2020 Framework Programme H2020-WIDESPREAD-01-2016-2017-TeamingPhase2 under grant agreement No. 739508, project CAMART2.

**Institutional Review Board Statement:** Not applicable.

**Informed Consent Statement:** Not applicable.

**Data Availability Statement:** The data presented are available on request from the corresponding author.

**Conflicts of Interest:** The authors declare no conflict of interest.

#### References

1. Zhang, H.; Liu, C.-X.; Qi, X.-L.; Dai, X.; Fang, Z.; Zhang, S.-C. Topological insulators in Bi<sub>2</sub>Se<sub>3</sub>, Bi<sub>2</sub>Te<sub>3</sub> and Sb<sub>2</sub>Te<sub>3</sub> with a single Dirac cone on the surface. *Nat. Phys.* **2009**, *5*, 438–442. [[CrossRef](#)]
2. Hsieh, D.; Xia, Y.; Wray, L.; Qian, D.; Pal, A.; Dil, J.H.; Osterwalder, J.; Meier, F.; Bihlmayer, G.; Kane, C.L.; et al. Observation of Unconventional Quantum Spin Textures in Topological Insulators. *Science* **2009**, *323*, 919–922. [[CrossRef](#)] [[PubMed](#)]
3. Hasan, M.Z.; Kane, C.L. Colloquium: Topological insulators. *Rev. Mod. Phys.* **2010**, *82*, 3045–3067. [[CrossRef](#)]

4. Fu, L.; Kane, C.L. Superconducting Proximity Effect and Majorana Fermions at the Surface of a Topological Insulator. *Phys. Rev. Lett.* **2008**, *100*, 096407. [[CrossRef](#)]
5. Fu, L.; Kane, C.L. Josephson current and noise at a superconductor/quantum-spin-Hall-insulator/superconductor junction. *Phys. Rev. B* **2009**, *79*, 161408. [[CrossRef](#)]
6. Manousakis, J.; Altland, A.; Bagrets, D.; Egger, R.; Ando, Y. Majorana qubits in a topological insulator nanoribbon architecture. *Phys. Rev. B* **2017**, *95*, 165424. [[CrossRef](#)]
7. Shiomi, Y.; Nomura, K.; Kajiwara, Y.; Eto, K.; Novak, M.; Segawa, K.; Ando, Y.; Saitoh, E. Spin-Electricity Conversion Induced by Spin Injection into Topological Insulators. *Phys. Rev. Lett.* **2014**, *113*, 196601. [[CrossRef](#)]
8. Khokhriakov, D.; Hoque, A.M.; Karpiak, B.; Dash, S.P. Gate-tunable spin-galvanic effect in graphene-topological insulator van der Waals heterostructures at room temperature. *Nat. Commun.* **2020**, *11*, 3657. [[CrossRef](#)]
9. Yasuda, K.; Mogi, M.; Yoshimi, R.; Tsukazaki, A.; Takahashi, K.S.; Kawasaki, M.; Kagawa, F.; Tokura, Y. Quantized chiral edge conduction on domain walls of a magnetic topological insulator. *Science* **2017**, *358*, 1311–1314. [[CrossRef](#)]
10. Xue, L.; Zhou, P.; Zhang, C.X.; He, C.Y.; Hao, G.L.; Sun, L.; Zhong, J.X. First-principles study of native point defects in Bi<sub>2</sub>Se<sub>3</sub>. *AIP Adv.* **2013**, *3*, 052105. [[CrossRef](#)]
11. Kunakova, G.; Surendran, A.P.; Montemurro, D.; Salvato, M.; Golubev, D.; Andzane, J.; Erts, D.; Bauch, T.; Lombardi, F. Topological insulator nanoribbon Josephson junctions: Evidence for size effects in transport properties. *J. Appl. Phys.* **2020**, *128*, 194304. [[CrossRef](#)]
12. Xu, Y.; Miotkowski, I.; Liu, C.; Tian, J.; Nam, H.; Alidoust, N.; Hu, J.; Shih, C.-K.; Hasan, M.Z.; Chen, Y. Observation of topological surface state quantum Hall effect in an intrinsic three-dimensional topological insulator. *Nat. Phys.* **2014**, *10*, 956–963. [[CrossRef](#)]
13. Hong, S.S.; Cha, J.J.; Kong, D.; Cui, Y. Ultra-low carrier concentration and surface-dominant transport in antimony-doped Bi<sub>2</sub>Se<sub>3</sub> topological insulator nanoribbons. *Nat. Commun.* **2012**, *3*, 757. [[CrossRef](#)]
14. Kunakova, G.; Galletti, L.; Charpentier, S.; Andzane, J.; Erts, D.; Léonard, F.; Spataru, C.D.; Bauch, T.; Lombardi, F. Bulk-free topological insulator Bi<sub>2</sub>Se<sub>3</sub> nanoribbons with magnetotransport signatures of Dirac surface states. *Nanoscale* **2018**, *10*, 19595–19602. [[CrossRef](#)]
15. Kunakova, G.; Bauch, T.; Palermo, X.; Salvato, M.; Andzane, J.; Erts, D.; Lombardi, F. High-Mobility Ambipolar Magnetotransport in Topological Insulator Bi<sub>2</sub>Se<sub>3</sub> Nanoribbons. *Phys. Rev. Appl.* **2021**, *16*, 024038. [[CrossRef](#)]
16. Brahlek, M.; Kim, Y.S.; Bansal, N.; Edrey, E.; Oh, S. Surface versus bulk state in topological insulator Bi<sub>2</sub>Se<sub>3</sub> under environmental disorder. *Appl. Phys. Lett.* **2011**, *99*, 012109. [[CrossRef](#)]
17. Veyrat, L.; Iacovella, F.; Dufouleur, J.; Nowka, C.; Funke, H.; Yang, M.; Escoffier, W.; Goiran, M.; Eichler, B.; Schmidt, O.G.; et al. Band Bending Inversion in Bi<sub>2</sub>Se<sub>3</sub> Nanostructures. *Nano Lett.* **2015**, *15*, 7503–7507. [[CrossRef](#)]
18. Brahlek, M.; Koirala, N.; Bansal, N.; Oh, S. Transport properties of topological insulators: Band bending, bulk metal-to-insulator transition, and weak anti-localization. *Solid State Commun.* **2015**, *215–216*, 54–62. [[CrossRef](#)]
19. Kong, D.; Cha, J.J.; Lai, K.; Peng, H.; Analytis, J.G.; Meister, S.; Chen, Y.; Zhang, H.-J.; Fisher, I.R.; Shen, Z.-X.; et al. Rapid Surface Oxidation as a Source of Surface Degradation Factor for Bi<sub>2</sub>Se<sub>3</sub>. *ACS Nano* **2011**, *5*, 4698–4703. [[CrossRef](#)]
20. Lang, M.; He, L.; Xiu, F.; Yu, X.; Tang, J.; Wang, Y.; Kou, X.; Jiang, W.; Fedorov, A.V.; Wang, K.L. Revelation of Topological Surface States in Bi<sub>2</sub>Se<sub>3</sub> Thin Films by In Situ Al Passivation. *ACS Nano* **2012**, *6*, 295–302. [[CrossRef](#)] [[PubMed](#)]
21. Ngabonziza, P.; Stehno, M.P.; Myoren, H.; Neumann, V.A.; Koster, G.; Brinkman, A. Gate-Tunable Transport Properties of In Situ Capped Bi<sub>2</sub>Te<sub>3</sub> Topological Insulator Thin Films. *Adv. Electron. Mater.* **2016**, *2*, 1600157. [[CrossRef](#)]
22. Andzane, J.; Kunakova, G.; Charpentier, S.; Hrkac, V.; Kienle, L.; Baitimirova, M.; Bauch, T.; Lombardi, F.; Erts, D. Catalyst-free vapour–solid technique for deposition of Bi<sub>2</sub>Te<sub>3</sub> and Bi<sub>2</sub>Se<sub>3</sub> nanowires/nanobelts with topological insulator properties. *Nanoscale* **2015**, *7*, 15935–15944. [[CrossRef](#)]
23. Singh, A. Growth, Structural and Electrical Characterization of Topological Dirac Materials. Ph.D. Thesis, University of Cambridge, Cambridge, UK, 28 June 2018.
24. Ghosh, R.; Kundu, S.; Majumder, R.; Roy, S.; Das, S.; Banerjee, A.; Guria, U.; Bera, M.K.; Subhedar, K.M.; Chowdhury, M.P.; et al. One-pot synthesis of multifunctional ZnO nanomaterials: Study of superhydrophobicity and UV photosensing property. *Appl. Nanosci.* **2019**, *9*, 1939–1952. [[CrossRef](#)]
25. Ashcroft, N.W.; Mermin, N.D. *Solid State Physics*; Harcourt College Publishers: San Diego, CA, USA, 1976.
26. Bansal, N.; Kim, Y.S.; Brahlek, M.; Edrey, E.; Oh, S. Thickness-Independent Transport Channels in Topological Insulator Bi<sub>2</sub>Se<sub>3</sub> Thin Films. *Phys. Rev. Lett.* **2012**, *109*, 116804. [[CrossRef](#)] [[PubMed](#)]
27. Qu, D.-X.; Hor, Y.S.; Xiong, J.; Cava, R.J.; Ong, N.P. Quantum Oscillations and Hall Anomaly of Surface States in the Topological Insulator Bi<sub>2</sub>Te<sub>3</sub>. *Science* **2010**, *329*, 821–824. [[CrossRef](#)] [[PubMed](#)]
28. Kunakova, G.; Meija, R.; Andzane, J.; Malinovskis, U.; Petersons, G.; Baitimirova, M.; Bechelany, M.; Bauch, T.; Lombardi, F.; Erts, D. Surface structure promoted high-yield growth and magnetotransport properties of Bi<sub>2</sub>Se<sub>3</sub> nanoribbons. *Sci. Rep.* **2019**, *9*, 11328. [[CrossRef](#)] [[PubMed](#)]